Electronic Supplementary Material (ESI) for Nanoscale Horizons.

Supplementary Information

Defect engineering enhances plasmonic-hot electrons exploitation for CO_2 reduction over polymeric catalysts

Hang Yin, ‡[ab] Zhehao Sun, ‡[a] Kaili Liu, ‡[a] Ary Anggara Wibowo,[c] Julien Langley,[a] Chao Zhang,[d] Sandra E. Saji,[a] Felipe Kremer,[e] Dmitri Golberg,[d] Hieu T. Nguyen,[c] Nicholas Cox,[a] Zongyou Yin*[ab]

[a] *Research School of Chemistry, Australian National University, ACT 2601, Australia. E-mail: zongyou.yin@anu.edu.au*

[b] *Institute for Climate, Energy & Disaster Solutions, Australian National University, ACT 2601, Australia*

[c] *School of Engineering, Australian National University, Canberra, Australian Capital Territory 2601, Australia*

[d] *Centre for Materials Science and School of Chemistry and Physics, Faculty of Science, Queensland University of Technology (QUT), 2 George Street, Brisbane, Queensland 4000, Australia*

[e] *Centre for Advanced Microscopy, Australian National University, Canberra, ACT 2601, Australia*

‡ These authors contributed equally.

Materials and Methods

Chemical and instrumentation

Light source is 300 W Xenon lamp from PerfectLight. Gas product was tested by Shimadzu GC-2030 equipped with FID and TCD detectors. Isotope labelling experiments were tested by GC: Agilent 7890B and MS: Agilent 7010 Triple Quad Electron Impact (EI) ionisation Low mass resolution MS/MS mode with collision induced dissociation (CID) for selective target quantifications. TEM images were recorded by JEOL 2100F FEGTEM. SEM images were recorded by Zeiss UltraPlus Field emission scanning electron microscope. XRD patterns were acquired by Bruker X-ray diffractometer (Cu Ka). EPR spectra were acquired by a Bruker E500 spectrometer equipped with a Bruker ER 4122 SHQE resonator.

Synthesis of g-C_3N_4-Ag

2 g of melamine was contained in a covered crucible and then heated to 550 ℃ in a muffle furnace for 3 hours with a heating rate of 20 ℃ min^{-1}. 20 mg of $AgNO_3$ and 20 mg g-C_3N_4 were dissolved in the mixture of 7.5 mL H_2O and 7.5 mL ethanol. Then, the suspension was degassed by N_2 with stirring for 30 min. Subsequently, the suspension was irradiated by solar under N_2 protection for 10 min, 1 hour, 3 hours, 5 hours. The product was washed by the mixture of H_2O and Ethanol for 3 times. Afterwards, the products were annealed at 400 ℃ under Argon protection with a ramping rate of 10 ℃ min^{-1}, to yield final products (g-C_3N_4-Ag-10m, g-C_3N_4-Ag-1h, g-C_3N_4-Ag-3h, and g-C_3N_4-Ag-5h).

Catalyst activity

5 mg of catalyst was dispersed in 5 mL 0.2 M $NaHCO_3$ aqueous solution to yield 1 mg/mL solution for liquid phase photocatalytic activity test. The solution was degassed by CO_2 for 30 min. In order to select the best catalyst for the following test, samples (g-C_3N_4, g-C_3N_4-Ag-10min, g-C_3N_4-Ag-1h, g-C_3N_4-Ag-3h, and g-C_3N_4-Ag-5h) were screened photocatalytic activity. After 24 hours photoirradiation, the best catalyst was selected for the plasmonic test.

Photo-to-charge conversion ability

5mg sample was dispersed in a solution which contains 950 μL ethanol and 50 μL, 5wt% Nafion, after sonicating 1h to form a homogeneous solution, took out 40 μL mixture and then dropped on FTO, respectively. The photocurrent was acquired by using the electrochemical workstation under the irradiation of light with AM 1.5G filter. The photo-to-electron conversion ability was analysed by corresponding photocurrent and the light intensities recorded by photometer.

The finite difference time domain (FDTD) simulations

The theoretical finite difference time domain (FDTD) simulations were performed by using Lumerical (FDTD solutions, Lumerical Solutions, Inc., Vancouver, Canada) software. The optical parameters of g-C_3N_4 used in FDTD simulation were calculated from the results of DFT calculations, and that of Ag were obtained from CRC materials database in Lumerical. We assumed that the background medium was the water with an index of refraction of 1.3. A total field-scattered

field (TFSF) source of light consisting of plane waves was used as the incident light source. A uniform grid size of 1 nm (x, y, and z) was accepted to ensure the accuracy of E-field calculations. A frequency-domain field distribution monitor was used to evaluate the E-field distribution. The perfectly matched layer (PML) absorbing boundary conditions was considered. The E-field magnitude from the incident light was received by following steps [1]:

$I_{ave} = c\epsilon_0 E_0^2/2$

$E_0 = (2I_{ave}/c\epsilon_0)^{1/2}$

where I_{ave} is the intensity of incident solar simulator (100 mW/cm^2), c is the speed of light, ε_0 is the permittivity of free space, and E_0 is the maximum E-field strength. The calculated E-field magnitude is 868 V/m.

Density functional theory (DFT) calculations

All DFT calculations were performed by using the Vienna ab initio Simulation Package (VASP) code [2]. Projector Augmented Wave (PAW) pseudopotentials [3] was used to process the core electrons and the Perdew-Burke-Ernzerhof (PBE) function of the generalized gradient approximation (GGA) [4] was used to describe electron exchange and related interactions. The cutoff energy of the plane wave basis set was 400 eV, and the convergence criteria for energy and force are less than 10^{-4} eV and 10^{-2} eV/Å, respectively. In addition, the van der Waals (vdW) correction was corrected for the dispersion correction using Grimme's DFT-D3 method [5] as implemented in VASP. For calculating optical properties, the Brillouin zone was sampled with 15 × 15 × 8 Monkhorst-Pack grids. The 2 × 2 × 1 supercells are used to construct slab model for calculating free energy to avoid the interactions caused by periodicity. The c direction was set to 40 Å to avoid interlayer interactions. The Brillouin zone was sampled with a 3 × 3 × 1 Monkhorst-Pack grids for calculating free energy.

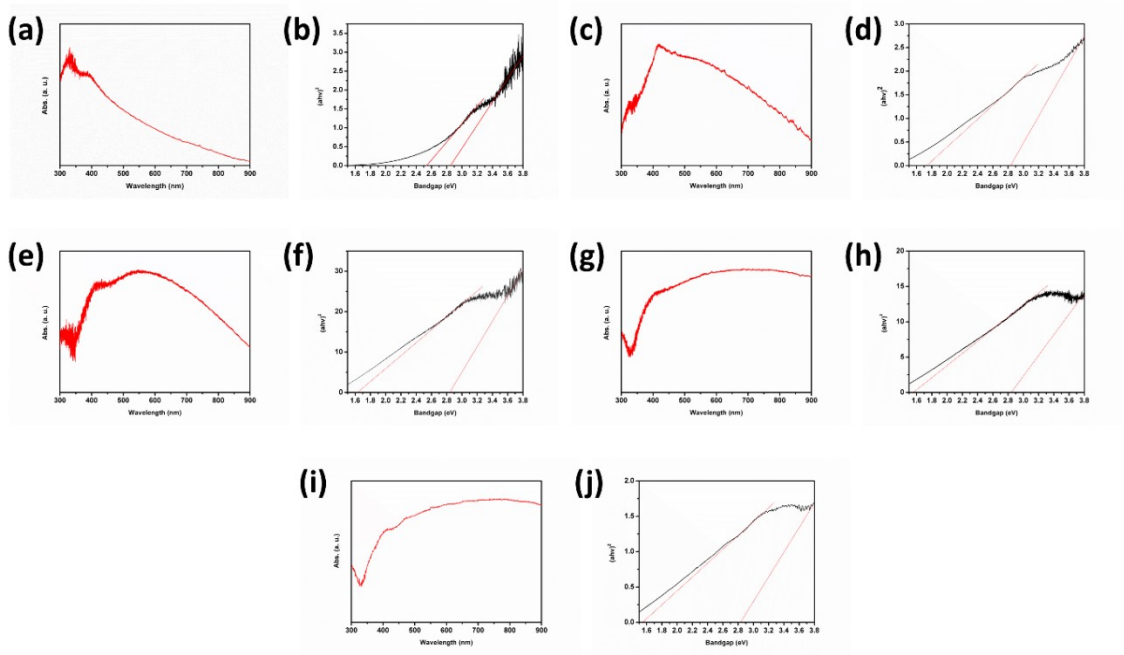

Fig. S1 UV-vis spectra and corresponding Tauc plot of (a, b) g-C_3N_4, (c, d) g-C_3N_4-Ag 10min, (e, f) g-C_3N_4-Ag 1h, (g, h) g-C_3N_4-Ag 3h, and (i, j) g-C_3N_4-Ag 5h.

Table S1. Bandgap and plasmonic energy of g-C_3N_4-Ag series catalysts.

Sample	Bandgap 1	Bandgap 2/ Plasmonic Energy
g-C_3N_4	2.84 eV	2.54 eV
g-C_3N_4-Ag 10m	2.84 eV	1.73 eV
g-C_3N_4-Ag 1h	2.84 eV	1.63 eV
g-C_3N_4-Ag 3h	2.84 eV	1.56 eV
g-C_3N_4-Ag 5h	2.84 eV	1.54 eV

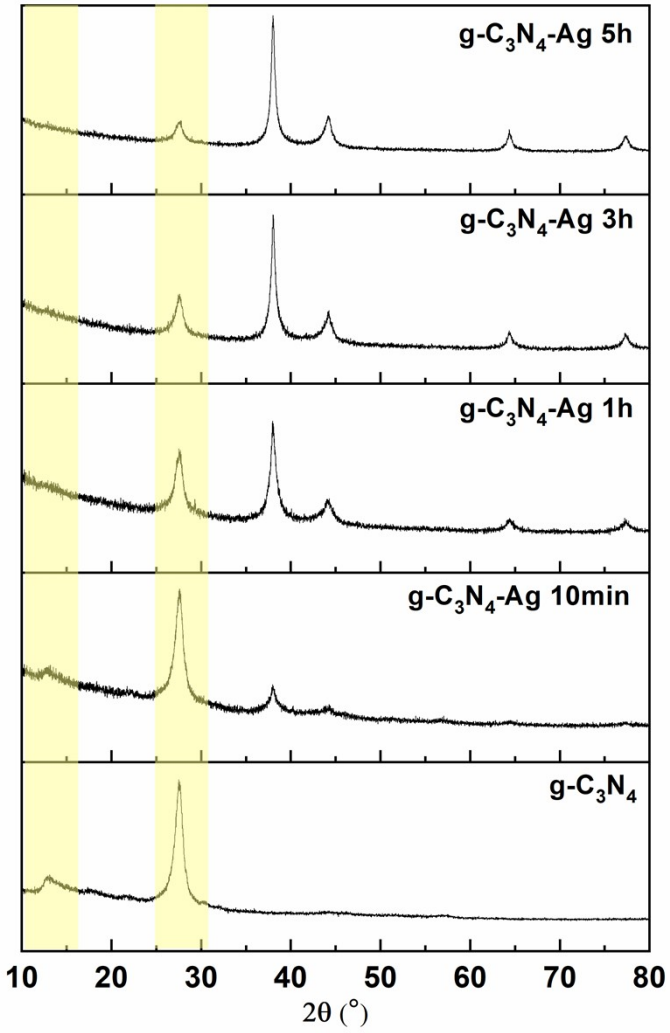

Fig. S2 XRD spectra of g-C_3N_4, g-C_3N_4-Ag 10min, g-C_3N_4-Ag 1h, g-C_3N_4-Ag 3h, and g-C_3N_4-Ag 5h, respectively. Highlight: peaks belong to g-C_3N_4.

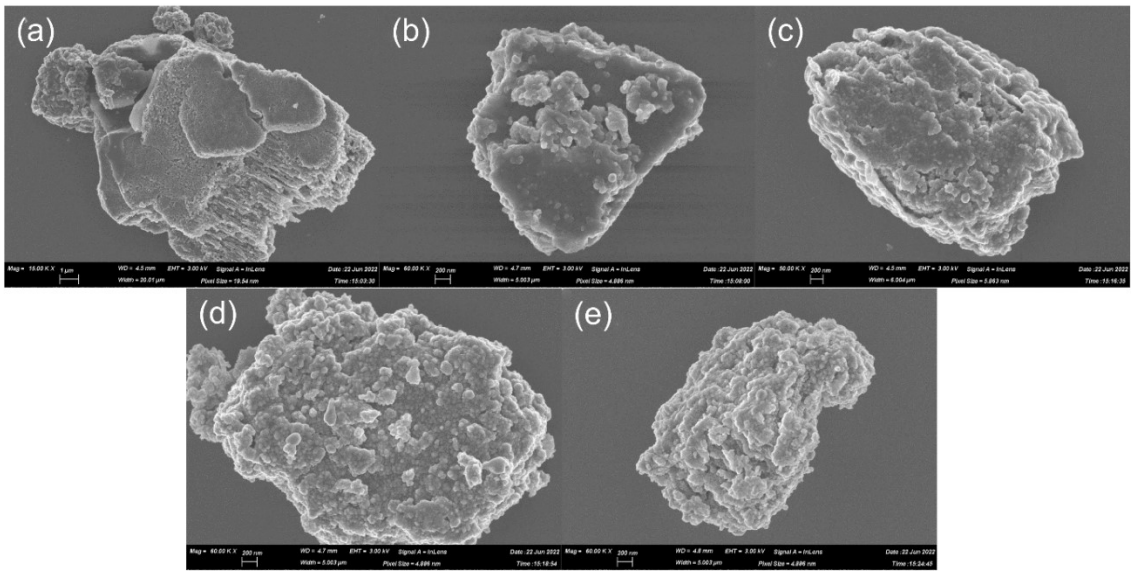

Fig. S3 SEM images of (a) g-C_3N_4, (b) g-C_3N_4-Ag 10min, (c) g-C_3N_4-Ag 1h, (d) g-C_3N_4-Ag 3h, and (e) g-C_3N_4-Ag 5h, respectively.

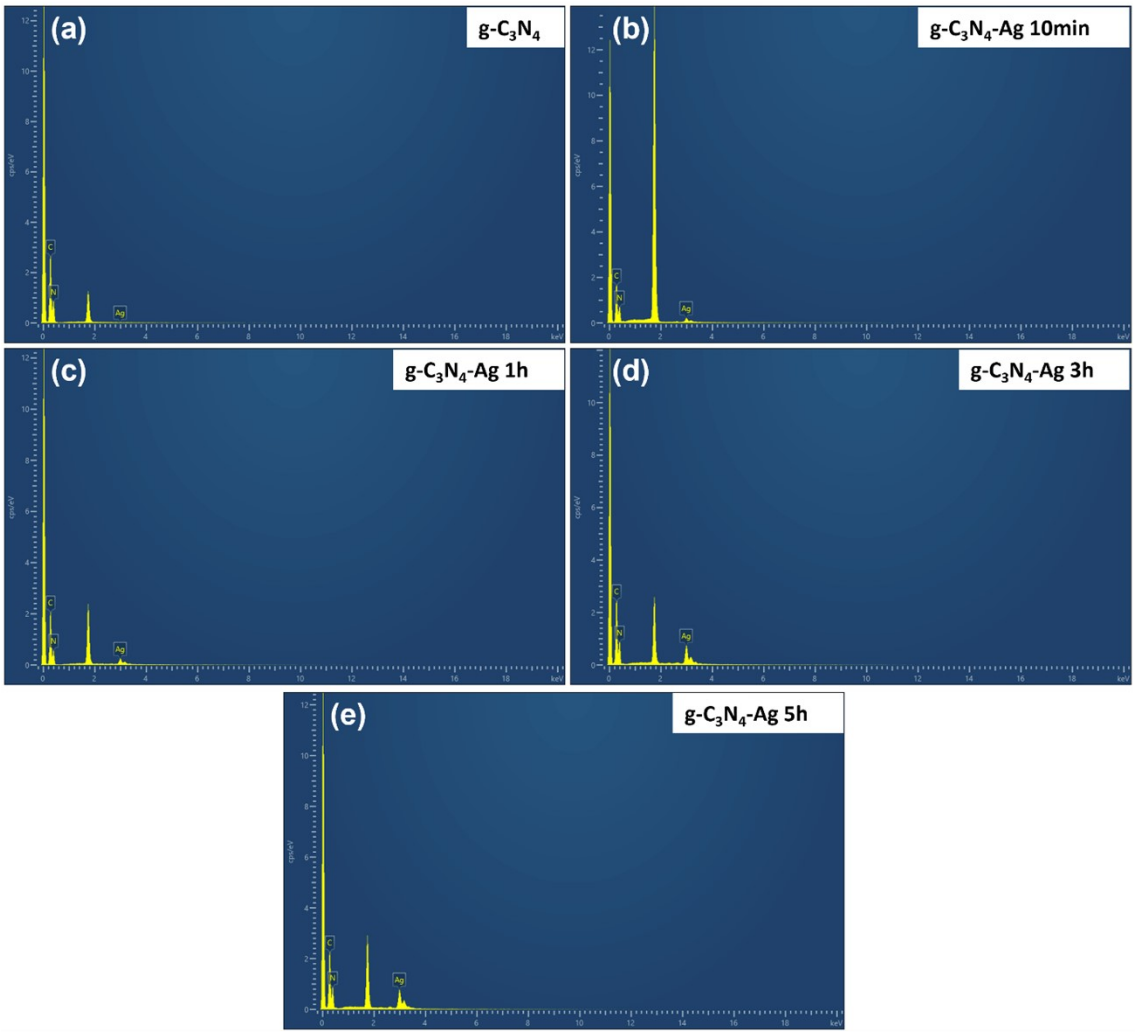

Fig. S4 SEM-EDS mapping of (a) g-C_3N_4, (b) g-C_3N_4-Ag 10min, (c) g-C_3N_4-Ag 1h, (d) g-C_3N_4-Ag 3h, and (e) g-C_3N_4-Ag 5h, respectively.

Table S2. Summary of Ag loading amount of g-C_3N_4-Ag catalysts.

Sample	Ag (wt%)
g-C_3N_4	0
g-C_3N_4-Ag 10m	1.24
g-C_3N_4-Ag 1h	1.82
g-C_3N_4-Ag 3h	5.14
g-C_3N_4-Ag 5h	6.29

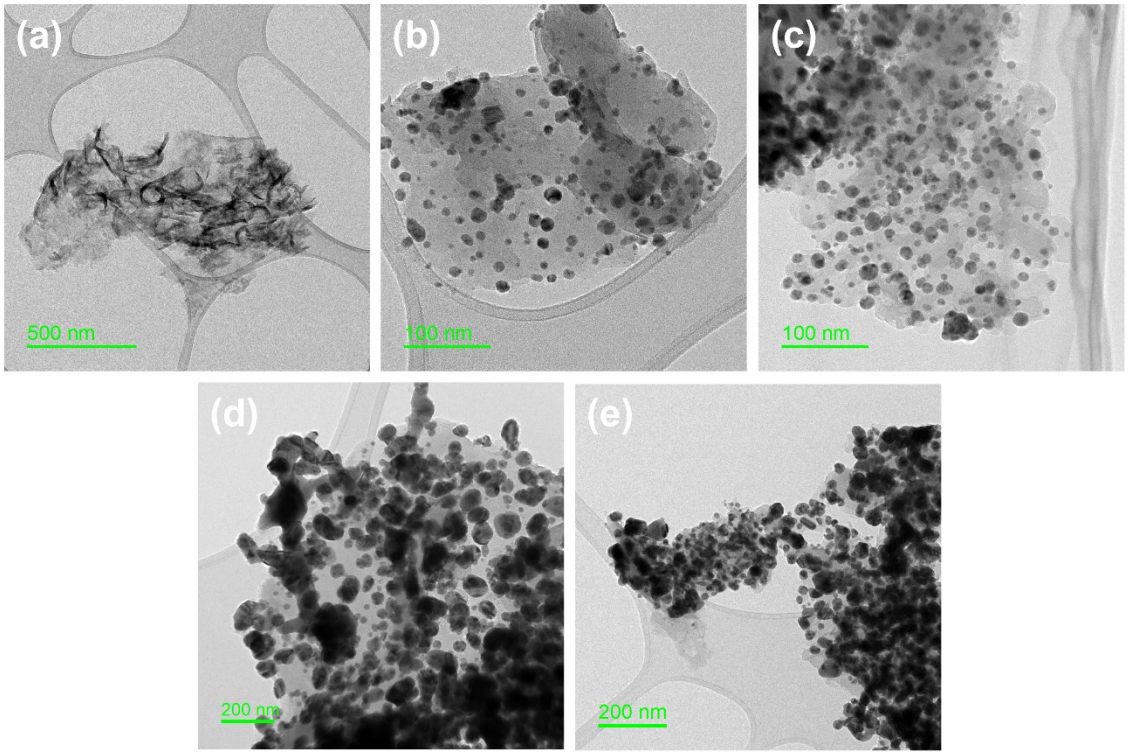

Fig. S5 TEM images of (a) g-C_3N_4, (b) g-C_3N_4-Ag 10min, (c) g-C_3N_4-Ag 1h, (d) g-C_3N_4-Ag 3h, and (e) g-C_3N_4-Ag 5h, respectively.

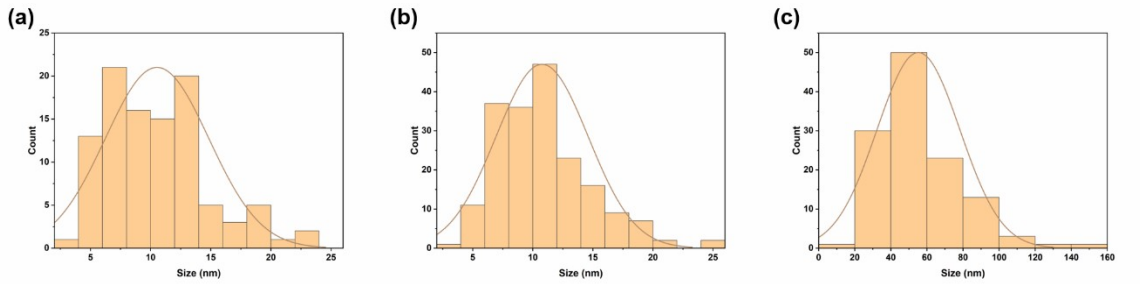

Fig. S6 Ag NPs size distribution of (a) g-C_3N_4-Ag 10min, (b) g-C_3N_4-Ag 1h, and (c) g-C_3N_4-Ag 3h yielded from TEM images.

Size distributions of Ag NPs of g-C_3N_4-Ag 10min (Fig. S6a), g-C_3N_4-Ag 1h (Fig. S6b), and g-C_3N_4-Ag 3h (Fig. S6c) have been analyzed according to their corresponding TEM images (Fig. S5). Compared with the average size of Ag NPs (10.54 nm) on g-C_3N_4-Ag 10min, the average size of Ag NPs (10.77 nm) on g-C_3N_4-Ag 1h has slightly increased, indicating that with shorter photodeposition time, it tends to produce new Ag NPs rather than the growth of exist Ag NPs. Whereas with longer photodeposition time, the Ag NPs (55.28 nm) on g-C_3N_4-Ag 3h grow larger, and merge adjacent Ag NPs to form even larger ones. Especially, merged Ag NPs on g-C_3N_4-Ag 5h cover most area of the surface of g-C_3N_4-Ag 5h, hence, it is hard to analyze its Ag NPs size distribution as other samples.

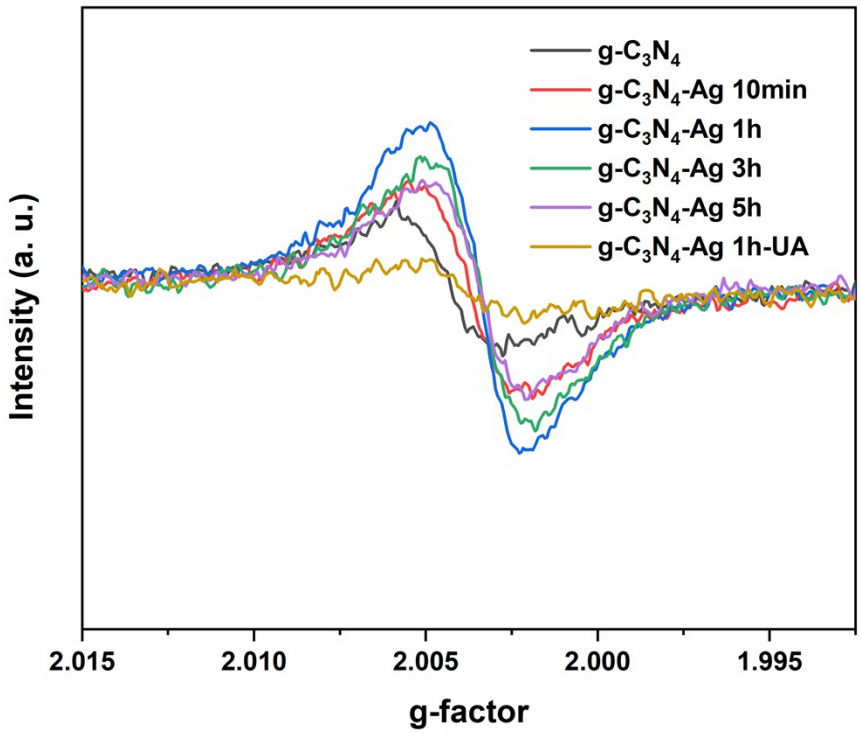

Fig. S7 EPR spectra monitored at 35 dB for g-C_3N_4, g-C_3N_4-Ag 10min, g-C_3N_4-Ag 1h, g-C_3N_4-Ag 3h, g-C_3N_4-Ag 5h, and g-C_3N_4-Ag 1h-UA, to validate the EPR spectra monitored at 15 dB in Fig. 2(a).

Table S3. Summary of g-factors of g-C_3N_4-Ag catalysts.

Sample	g-factor
g-C_3N_4	2.0044
g-C_3N_4-Ag 10m	2.0037
g-C_3N_4-Ag 1h	2.0034
g-C_3N_4-Ag 3h	2.0034
g-C_3N_4-Ag 5h	2.0035
g-C_3N_4-Ag 1h-UA	2.0042

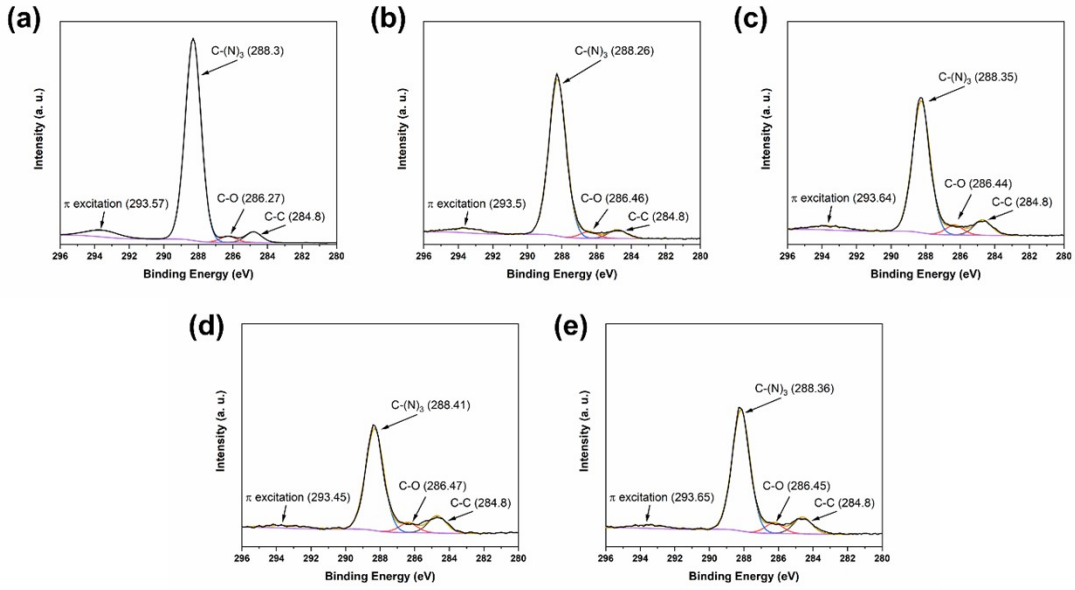

Fig. S8 C1s spectra yielded from XPS of (a) g-C_3N_4, (b) g-C_3N_4-Ag 10min, (c) g-C_3N_4-Ag 1h, (d) g-C_3N_4-Ag 3h, and (e) g-C_3N_4-Ag 5h, respectively.

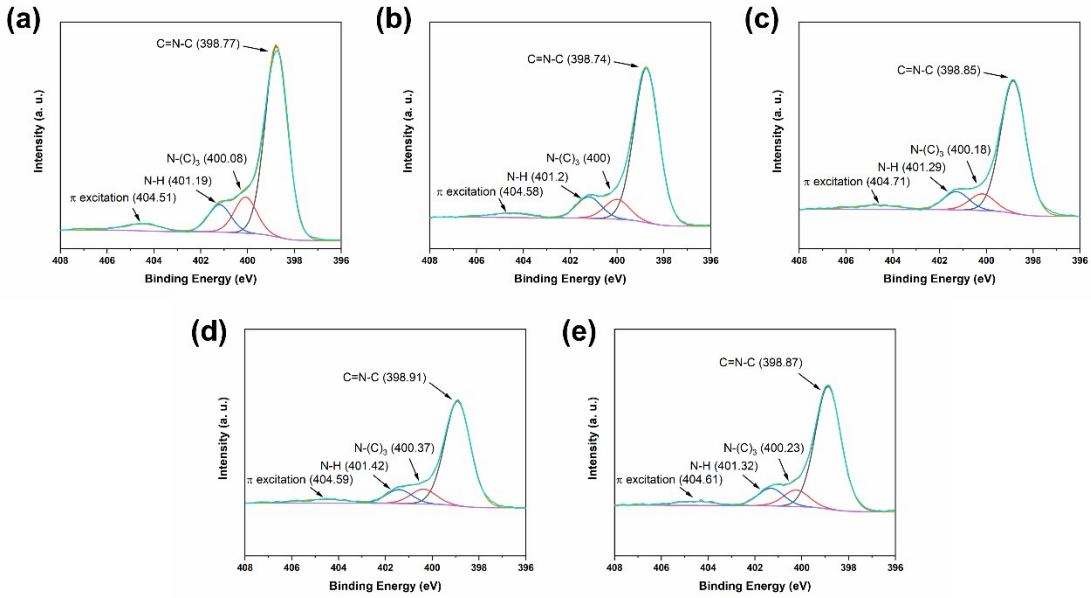

Fig. S9 N1s spectra yielded from XPS of (a) g-C_3N_4, (b) g-C_3N_4-Ag 10min, (c) g-C_3N_4-Ag 1h, (d) g-C_3N_4-Ag 3h, and (e) g-C_3N_4-Ag 5h, respectively.

Table S4. Atomic ratio and C/N ratio yielded from XPS results.

	$g\text{-}C_3N_4$	$g\text{-}C_3N_4$-Ag 10m	$g\text{-}C_3N_4$-Ag 1h	$g\text{-}C_3N_4$-Ag 3h	$g\text{-}C_3N_4$-Ag 5h
C-C	1.90 %	1.93 %	3.66 %	4.75 %	4.11 %
C-O	1.08 %	1.44 %	2.29 %	2.69 %	2.55 %
$C\text{-}(N)_3$	35.85 %	34.24 %	31.40 %	28.23 %	29.69 %
C-π excitation	2.49 %	2.00 %	1.98 %	1.65 %	1.57 %
C=N-C	40.96 %	41.20 %	38.76 %	35.33 %	37.18 %
$N\text{-}(C)_3$	7.75 %	5.32 %	4.89 %	4.99 %	5.01 %
N-H	5.89 %	5.73 %	5.33 %	4.69 %	5.35 %
N-π excitation	2.57 %	1.89 %	2.17 %	2.35 %	1.95 %
C/N ratio	0.723	0.736	0.769	0.788	0.766

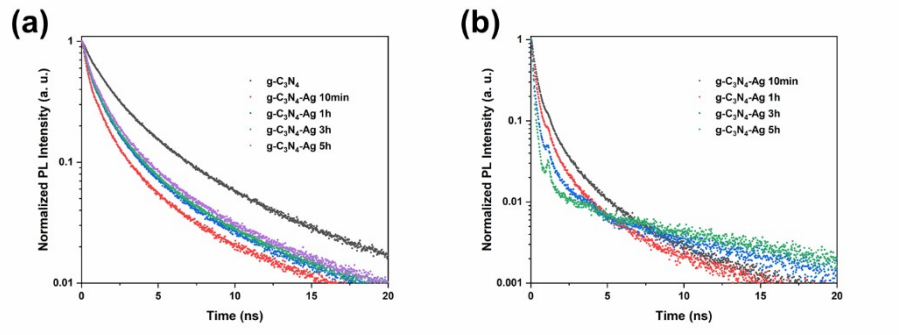

Fig. S10 (a) TRPL spectra of defects in g-C_3N_4, g-C_3N_4-Ag 10min, g-C_3N_4-Ag 1h, g-C_3N_4-Ag 3h, and g-C_3N_4-Ag 5h excited at 375 nm and recorded at 488 nm. (b) TRPL spectra of Ag in g-C_3N_4-Ag 10min (excited at 485 nm and recorded at 716 nm), g-C_3N_4-Ag 1h (excited at 485 nm and recorded at 770 nm), g-C_3N_4-Ag 3h (excited at 485 nm and recorded at 800 nm), and g-C_3N_4-Ag 5h (excited at 485 nm and recorded at 805 nm).

In addition to the TRPL results of pristine g-C_3N_4 in the absence and in the presence of different amount of Ag, the TRPL results of defects from the corresponding samples were also monitored (Fig. S8a). The data indicates the electrons excited to the defects of g-C_3N_4-Ag 10min can be separated better than the defects from other samples. However, since the deficient of defects of g-C_3N_4-Ag 10min, its catalytic activity still cannot compete with the g-C_3N_4-Ag 1h, the one has the most balanced defects number and electron generation ability. The TRPL results for the plasmonic excitation (Fig. S8b) were also tested. The longer emission wavelength of samples showed a shorter average lifetime of PL, which can be ascribed to the nonradiative recombination such as lattice vibration, and phonon exchanging thermal energy with the catalysts.[6]

Table S5. Summary of TRPL results of g-C_3N_4-Ag catalysts.

Sample	Excitation-Emission	t1 (ns)	t2 (ns)	Average Lifetime (ns)
g-C_3N_4	375 nm - 420 nm	0.915	4.821	1.425
	375 nm - 488 nm	1.747	7.978	2.990
g-C_3N_4-Ag 10min	375 nm - 420 nm	0.371	2.760	0.569
	375 nm - 488 nm	0.868	6.139	1.542
	485 nm - 716 nm	0.290	2.354	0.379
g-C_3N_4-Ag 1h	375 nm - 420 nm	0.394	2.754	0.618
	375 nm - 488 nm	1.045	6.454	1.828
	485 nm - 770 nm	0.191	2.165	0.232
g-C_3N_4-Ag 3h	375 nm - 420 nm	0.400	2.642	0.610
	375 nm - 488 nm	1.077	6.634	1.899
	485 nm - 800 nm	0.091	5.287	0.101
g-C_3N_4-Ag 5h	375 nm - 420 nm	0.514	3.017	0.883
	375 nm - 488 nm	1.174	7.179	2.043
	485 nm - 805 nm	0.022	10.880	0.025

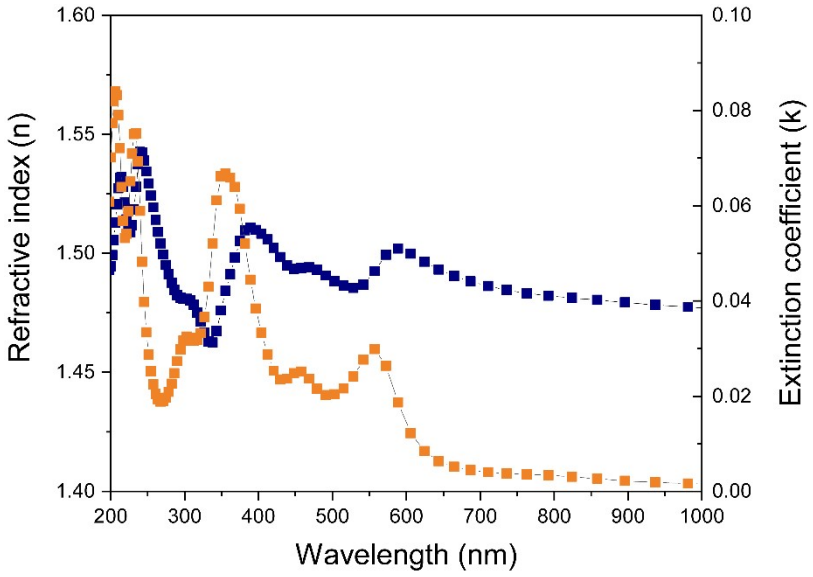

Fig. S11 Refractive index (n) and extinction coefficient (k) along the z direction versus wavelength of g-C_3N_4 used in Finite-difference Time-domain (FDTD) electric field simulation.

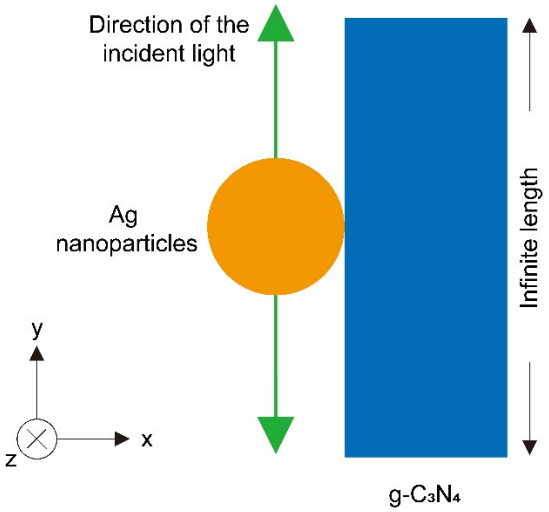

Fig. S12 The model diagram used for Finite-difference Time-domain (FDTD) electric field simulation.

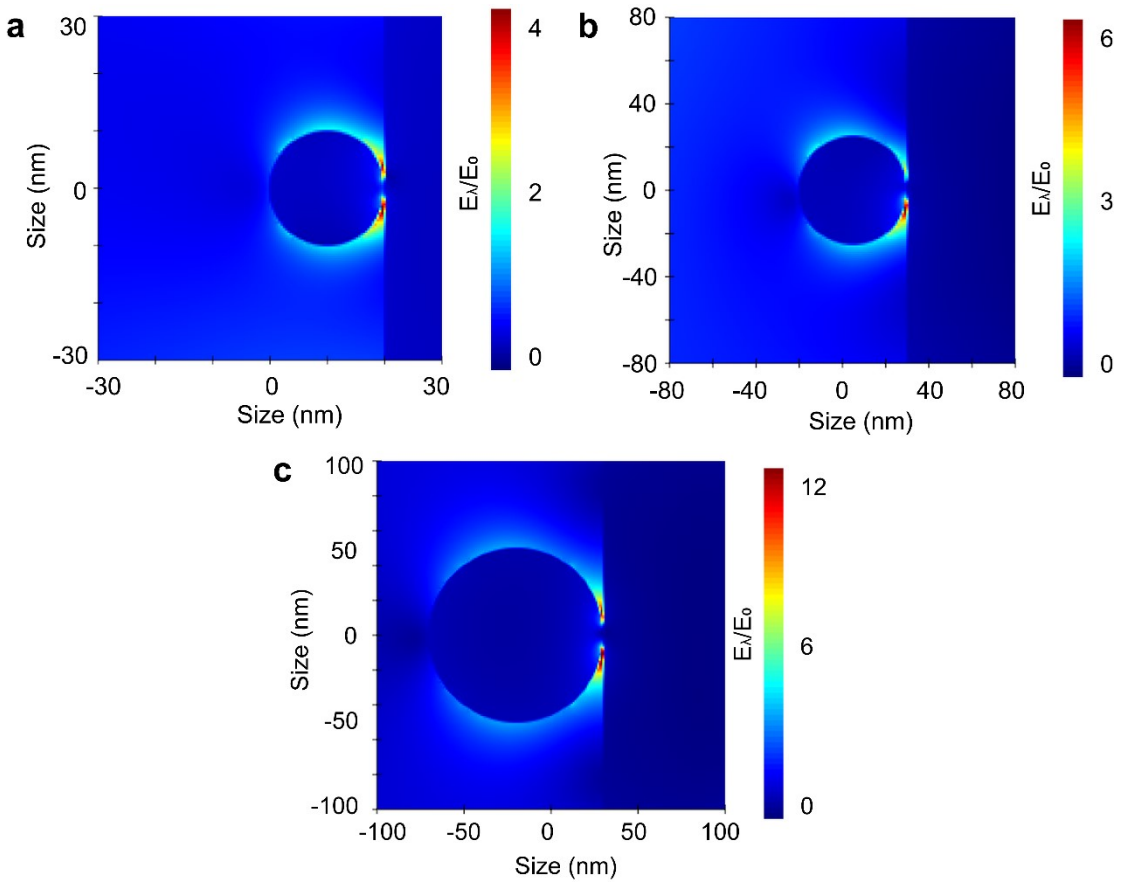

Fig. S13 Finite-difference Time-domain (FDTD) electric field simulation analysis. The FDTD electric field simulation results for diameters of (a) 20 nm, (b) 50 nm and (c) 100 nm Ag nanoparticles of the incident light relative. The FDTD electric field simulation results for wavelengths from 300 nm to 1000 nm of the incident light.

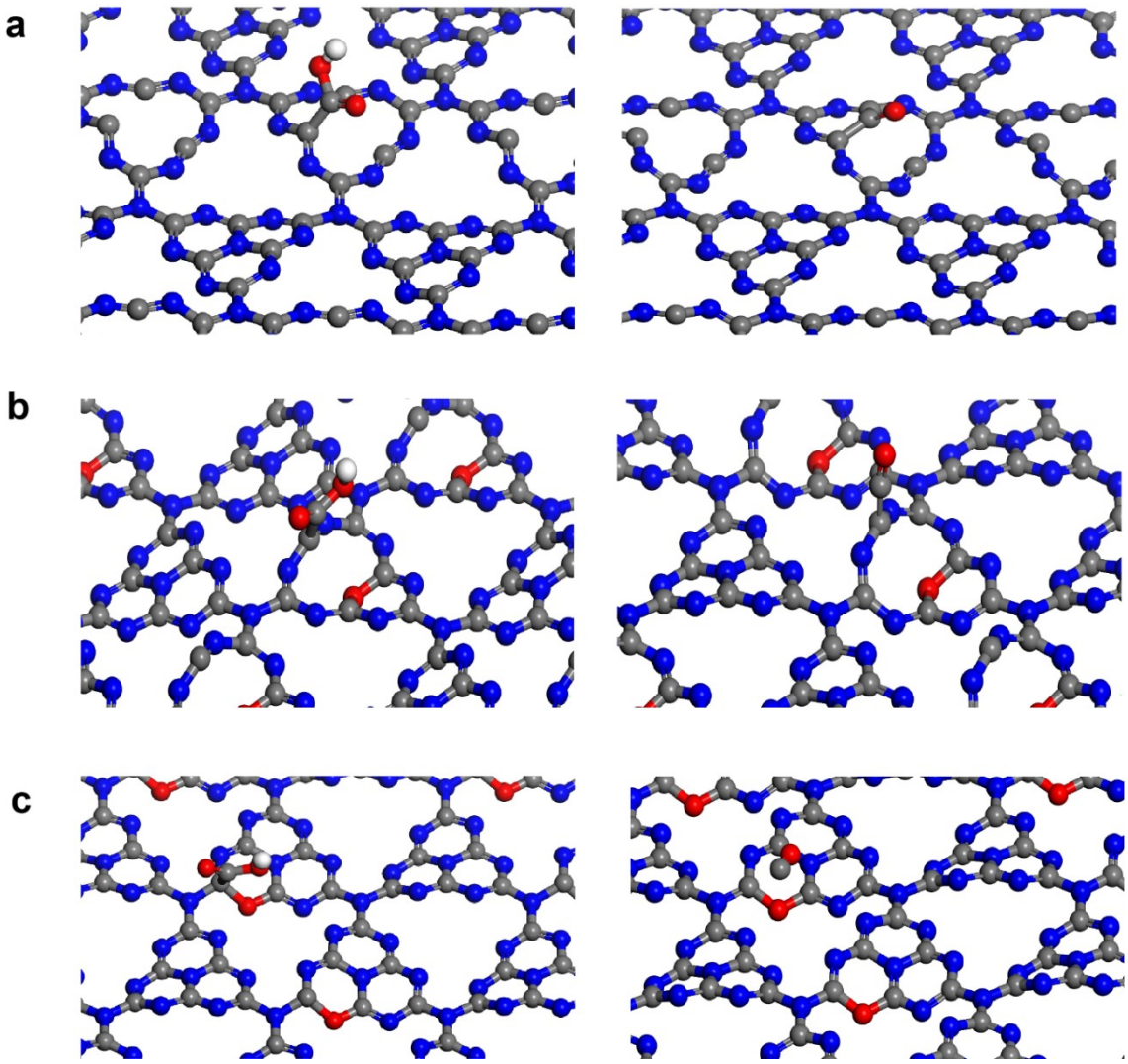

Fig. S14 Optimized configurations of reaction intermediates *COOH and *CO on the C atom and N vacancy active sites of (a) g-C_3N_4 with N vacancy, (b) middle and (c) side O-occupied g-C_3N_4 (Red: O; white: H; gray: C; blue: N) by DFT calculation.

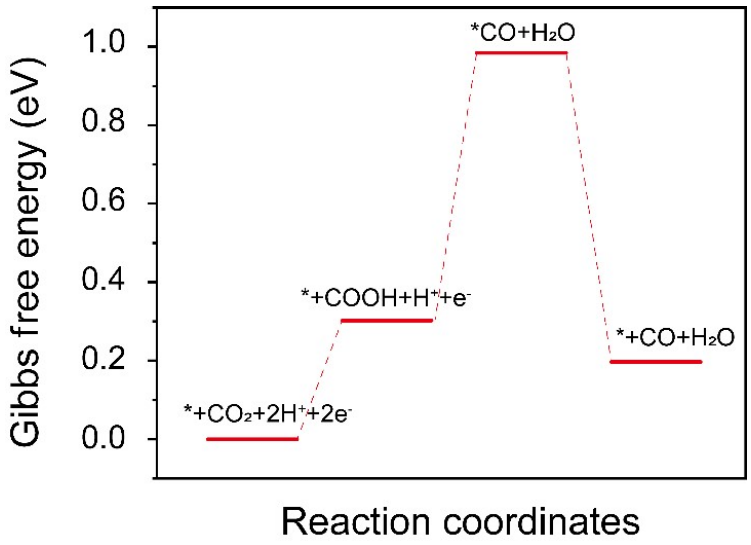

Fig. S15 Free energy diagram for photocatalytic CO_2 reduction to CO on side O-occupied g-C_3N_4 calculated by DFT.

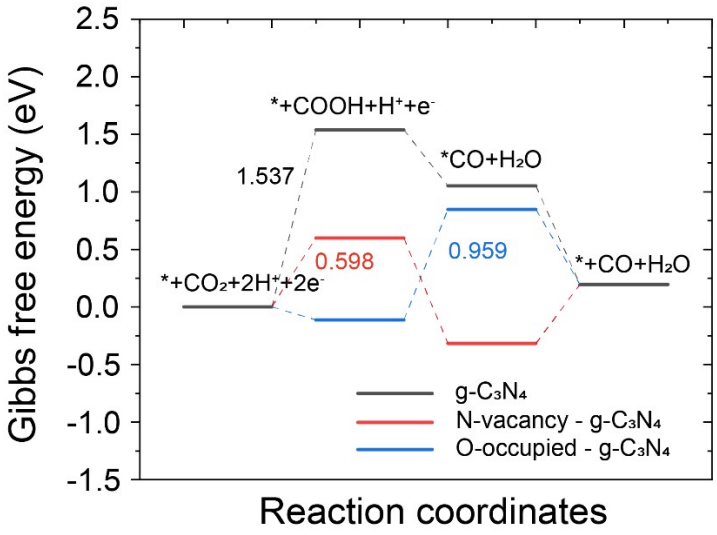

Fig. S16 Free energy diagram for photocatalytic CO_2 reduction to CO on g-C_3N_4, g-C_3N_4 with N vacancy and O-occupied g-C_3N_4 under electric field (E=10415 V/m).

Table S6. Summary of ΔG of different structures in the absence and in the presence of electric field.

Structure name	$\triangle G_{COOH}$	$\triangle G_{CO}$
g-C_3N_4	1.535	-0.486
g-C_3N_4 electric field	1.537	-0.485
N-vacancy g-C_3N_4	0.597	-0.915
N-vacancy g-C_3N_4 electric field	0.598	-0.915
O-occupied g-C_3N_4	-0.113	0.959
O-occupied g-C_3N_4 electric field	-0.112	0.959

References

(1) Hecht, E., Optics 2nd edition Addison. Wesley Publishing Company1987.

(2) (a) Kresse, G.; Furthmüller, J. Efficiency of ab-initio total energy calculations for metals and semiconductors using a plane-wave basis set. *Computational materials science* **1996,** *6*, 15-50. (b) Kresse, G.; Furthmüller, J. Efficient iterative schemes for ab initio total-energy calculations using a plane-wave basis set. *Physical review B* **1996,** *54*, 11169.

(3) Blöchl, P. E. Projector augmented-wave method. *Physical review B* **1994,** *50*, 17953.

(4) Perdew, J. P.; Burke, K.; Ernzerhof, M. Generalized gradient approximation made simple. *Physical review letters* **1996,** *77*, 3865.

(5) Grimme, S.; Antony, J.; Ehrlich, S.; Krieg, H. A consistent and accurate ab initio parametrization of density functional dispersion correction (DFT-D) for the 94 elements H-Pu. *The Journal of chemical physics* **2010,** *132*, 154104.

(6) (a) Shockley, W.; Read, W. T. Statistics of the Recombinations of Holes and Electrons. *Physical Review* **1952,** *87*, 835-842. (b) Hall, R. N. Electron-Hole Recombination in Germanium. *Physical Review* **1952,** *87*, 387-387.